DC voltage droop control design for multi-terminal HVDC systems considering AC and DC grid dynamics

Eduardo Prieto-Araujo, *Graduate Student Member, IEEE*, Agustí Egea-Alvarez, *Member, IEEE*, Sajjad (Fekri) Fekriasl, *Member, IEEE*, Oriol Gomis-Bellmunt, *Senior Member, IEEE*

***Abstract*—This article is focused on the droop-based DC voltage control design for multi-terminal VSC-HVDC grid systems, considering the AC and the DC system dynamics. The droop control design relies on detailed linearized models of the complete multi-terminal grid, including the different system dynamics, such as the DC grid, the AC grid, the AC connection filters and the converter inner controllers. Based on the derived linear models, classical and modern control techniques are applied to design the different controllers, including a multi-variable frequency analysis to design the grid voltage droop control. In combination with the droop control, a DC oscillation damping scheme is proposed, in order to improve the system performance. The control design is validated through simulations of a three-terminal system.**

***Index Terms*—Offshore wind power, multi-terminal, droop control, HVDC, AC and DC grid interactions.**

I. Introduction

In the North Sea, a number of wind power plants are being commissioned due to the abundant wind resource and the shallow waters [1]. However, offshore installations present some financial and technical challenges [2], such as long distance transmission systems required for the energy grid integration. Currently, High Voltage Direct Current (HVDC) systems based on Voltage Source Converters (VSC) are being installed for integrating the energy of individual offshore wind power plants to the main land AC grid. Moreover, as the number of offshore wind farm projects to be connected to the land through VSC-HVDC is increasing, the idea of interconnecting these systems in a multi-terminal grid topology to increase the flexibility of the system becomes interesting [3].

The multi-terminal VSC-HVDC grid concept poses several challenges as the technology of the different elements connected to the system is still evolving in terms of power and voltage levels. Among other problems, the control of the DC voltage of multi-terminal VSC-HVDC grids has become a priority, in order to ensure the overall grid system stability. The operation of the DC grid employing a hierarchical scheme has been proposed in [4], considering the well-known droop as the primary control, operated together with a secondary control to establish the desired power flow. In particular, the droop control is an accepted solution to regulate the DC grid voltage fast, also allowing to establish a power sharing between the different converters connected to the grid [5]. Different implementations of the droop control, mainly current or power based, can be found in the literature [6]. Regarding the controller design, it has been addressed in different studies. In [7], the controller tuning is based on the steady state characteristics and the resulting power flow sharing [8]. In [9] the influence of the DC grid dynamics and DC grid operational limitations are considered during the design stage. In [10] the droop control is tuned considering the effect of the DC cable dynamics. In [11], a droop design to reduce the perturbations of the DC system over the AC grid is explained and in [12], the droop control is designed based on a trade-off between the power losses, the desired power flow and the minimization of voltage deviations.

In this work, the power-based droop control is designed considering the complete multi-terminal grid dynamics, including the linearized DC grid and AC grid dynamics, the converter controllers, and a DC oscillation damping loop, expanding the scope of previous work [9], which was mainly focused on designing a current-based droop through a linear DC grid dynamic analysis. In order to analyze the mentioned system dynamics, a linearized model of the complete multi-terminal VSC-HVDC grid is derived. Then, based on the linear model obtained, the system dynamics are analyzed employing multi-variable frequency methods to select suitable droop controllers for the DC grid. The theoretical developments are validated through simulations in a three-terminal grid.

The paper is organized as follows. The next section describes the droop control operation of multi-terminal VSC-HVDC grids. Section III presents the derivation of the linear model of a generic multi-terminal HVDC grid. The control design methodology is described in Section IV and in Section V, the control design strategy is applied to a three-terminal grid. Finally, in Section VI the article conclusions are drawn.

II. Multi-terminal grid control

A generic VSC-HVDC multi-terminal grid layout is shown in Fig. 1. The HVDC grid is built to interconnect the offshore

Mr. Prieto-Araujo, Dr. Egea-Alvarez and Dr. Gomis-Bellmunt are with the Departament d'Enginyeria Elèctrica, Centre d'Innovació Tecnològica en Convertidors Estàtics i Accionaments (CITCEA-UPC), Universitat Politècnica de Catalunya. ETS d'Enginyeria Industrial de Barcelona, Barcelona, Spain. (e-mail: eduardo.prieto-araujo@citcea.upc.edu)

Dr. Fekriasl is with the Advanced Research and Technology Centre, Alstom Grid, Stafford, UK.

This work has been funded by the Spanish Ministry of Economy and Competitiveness under the projects ENE2012-33043 and ENE2013-47296. This research was co-financed by the European Regional Development Fund (ERDF).

wind power plants and the main land AC grid or grids by means of VSC power converters. Wind Farm Converters (WFC) inject the generated power from the wind power plants to the DC grid, whereas the Grid Side Converters (GSC) regulate the DC grid voltage employing droop control [5], [13].

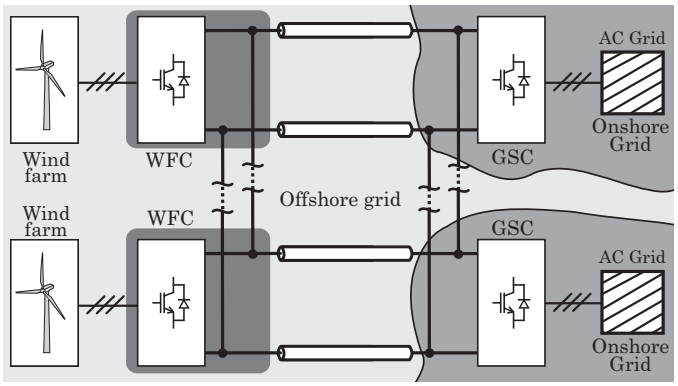

Figure 1. VSC-HVDC multiterminal grid

This type of controller allows to regulate the DC grid voltage without communications among converters, being implemented at each of the GSCs locally. Also, droop control allows to establish the power sharing between converters acting over the power loop of the converter, as it is shown in Fig. 2. Possible deviations of the power, can be compensated through an upper secondary control [4], that could be implemented with communications between the grid converters (Fig. 2), acting in a slower time frame. In this work, this upper controller is not included in the analysis, as the study is mainly focused on the grid voltage control based on droop, considering the overall grid dynamics. The droop control law, implemented in the n different GSCs is:

$$P^* = K(E - E^*) \tag{1}$$

where E is the voltage measured at the DC terminals of the GSC converter, E^* is the voltage reference for the droop controller, K is the droop constant and P^* is the power reference introduced to the power loop. Based on the power set-point, the power controller (G_P) regulates the power flowing through the converter in order to track the DC grid voltage reference, even assuming a DC voltage error due to the proportional nature of the droop controller. Regarding the AC voltage, it is controlled by means of an AC module voltage regulator (G_U). The outputs of the power and AC voltage regulators are connected to the inner conventional current loop, that will apply voltages to the AC grid by means of the power converter, in order to regulate both current references.

Dynamics of the different interconnected systems could affect the droop voltage regulation, such as the DC multi-terminal grid, the AC grid connection points, the AC grid converter filter, the power and voltage controllers or the current inner control. Then, the design of the droop voltage control should be performed considering the mentioned dynamics in order to ensure a proper control performance. To do so, in this work a complete linear model of the multi-terminal grid is

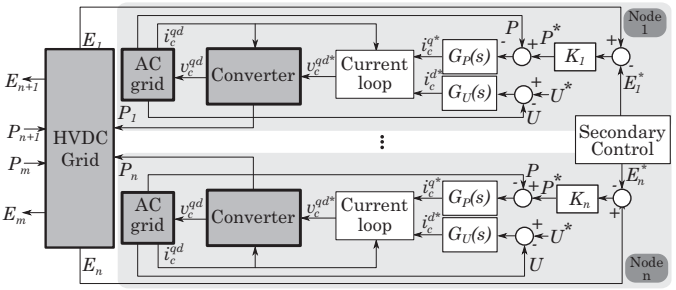

Figure 2. Multi-terminal control structure including DC and AC dynamics

derived. Once the model is obtained, the different controllers, including the droop voltage control, are designed combining classical and modern control techniques.

III. System modelling

In this section, the procedure to obtain a linear model of a generic multi-terminal grid (Fig. 1), is detailed. The complete model is divided in two parts, the AC system and the DC system. Regarding the AC system, the linearized equations of a GSC connected to an AC grid are described. On the other hand, the linearized DC grid model is derived for a simple DC link and the procedure to model a larger grid is included. The existing link between both models is the power converter. It is modeled employing three voltage sources in the AC side and a dependent current source in the DC side, without considering losses or Modular Multilevel Converter (MMC) inner dynamics.

A. AC system

In this section, the model of a VSC-HVDC converter connected to the grid is addressed. The converter grid connection is performed by either an inductance (L) or an inductance and capacitor filter (LC) depending on the application [14], [15], as it is shown in Fig. 3.

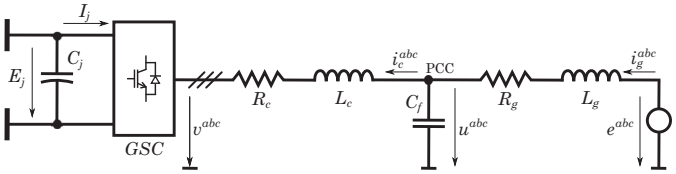

Figure 3. Model of the converter connection to the AC grid

Regarding the AC grid connection, it is represented through a simple Thévenin equivalent. The state-space model of the converter grid connection considering the LC filter is:

$$\frac{dx_{lc}}{dt} = \mathbf{A_{lc}} x_{lc} + \mathbf{B_{lc}} u_{lc} \tag{2}$$

where A_{lc} and B_{lc} are:

$$\mathbf{A_{lc}} = \begin{pmatrix} -\frac{R_c}{L_c} & -\omega & \frac{1}{L_c} & 0 & 0 & 0 \\ \omega & -\frac{R_c}{L_c} & 0 & \frac{1}{L_c} & 0 & 0 \\ -\frac{1}{C_f} & 0 & 0 & -\omega & \frac{1}{C_f} & 0 \\ 0 & -\frac{1}{C_f} & \omega & 0 & 0 & \frac{1}{C_f} \\ 0 & 0 & -\frac{1}{L_g} & 0 & -\frac{R_g}{L_g} & -\omega \\ 0 & 0 & 0 & -\frac{1}{L_g} & \omega & -\frac{R_g}{L_g} \end{pmatrix} \tag{3}$$

$$\mathbf{B_{lc}} = \begin{pmatrix} -\frac{1}{L_c} & 0 & 0 & 0 \\ 0 & -\frac{1}{L_c} & 0 & 0 \\ 0 & 0 & 0 & 0 \\ 0 & 0 & 0 & 0 \\ 0 & 0 & \frac{1}{L_g} & 0 \\ 0 & 0 & 0 & \frac{1}{L_g} \end{pmatrix} \quad (4)$$

where L_c is the filter inductance value and R_c its parasitic resistance, ω is the frequency of the grid, C_f is the capacitance of the capacitor filter and L_g and R_g are the inductance and resistance of the grid Thévenin equivalent. The state and input vectors are:

$$x_{lc} = (i_c^q, i_c^d, u^q, u^d, i_g^q, i_g^d) \quad (5)$$

$$u_{lc} = (v^q, v^d, e^q, e^d) \quad (6)$$

where i_c^{qd} are the currents flowing from the Point of Common Coupling (PCC) to the converter, i_g^{qd} are the currents flowing to the grid, e^{qd} are the grid voltages, u^{qd} are the voltages at the PCC and v^{qd} are the voltages applied by the converter, in the synchronous reference frame. Applying linearization to the previous equations, the state-space representation can be expressed as:

$$\frac{d\Delta x_{lc}}{dt} = \mathbf{A_{lc}}\Delta x_{lc} + \mathbf{B_{lc}}\Delta u_{lc} \quad (7)$$

$$\Delta y_{lc} = \mathbf{C_{lc}}\Delta x_{lc} + \mathbf{D_{lc}}\Delta u_{lc} \quad (8)$$

where the matrix $\mathbf{A_{lc}}$ and $\mathbf{B_{lc}}$ are the matrices defined in (3) and (4). Regarding, the system output equation, matrices $\mathbf{C_{lc}}$ and $\mathbf{D_{lc}}$ are:

$$\mathbf{C_{lc}} = \left(\begin{array}{cccccc} \multicolumn{6}{c}{\mathbf{I_{6x6}}} \\ \hline 0 & 0 & \frac{u_0^q}{U_0} & \frac{u_0^d}{U_0} & 0 & 0 \\ 0 & 0 & \frac{3\,i_{g0}^q}{2} & \frac{3\,i_{g0}^d}{2} & \frac{3\,u_0^q}{2} & \frac{3\,u_0^d}{2} \\ \frac{3\,v_{g0}^q}{2} & \frac{3\,v_{g0}^d}{2} & 0 & 0 & 0 & 0 \end{array} \right) \quad (9)$$

$$\mathbf{D_{lc}} = \left(\begin{array}{cccc} \multicolumn{4}{c}{\mathbf{0_{8x4}}} \\ \hline \frac{3\,i_{c0}^q}{2} & \frac{3\,i_{c0}^d}{2} & 0 & 0 \end{array} \right) \quad (10)$$

where $\mathbf{I_{6x6}}$ is a 6x6 identity matrix and $\mathbf{0_{8x4}}$ is a zero matrix of 8 rows and 4 columns. The linearized state variables, inputs and outputs are:

$$\Delta u_{lc} = (\Delta v^q, \Delta v^d, \Delta e^q, \Delta e^d) \quad (11)$$

$$\Delta y_{lc} = (\Delta i_c^q, \Delta i_c^d, \Delta u^q, \Delta u^d, \Delta i_g^d, \Delta i_g^d, \Delta U, \Delta P_u, \Delta P)$$

where U is the PCC voltage magnitude, P_u is the power flowing to the AC grid, P is the power flowing through the converter and v_0^{qd}, u_0^{qd}, i_{c0}^{qd}, i_{g0}^{qd} and U_0 are the system variables at the linearization point. Note also that, the Park transformation used for this system is [16]:

$$\mathbf{T}(\theta) = \frac{3}{2} \begin{pmatrix} \cos(\theta) & \cos(\theta - \frac{2\pi}{3}) & \cos(\theta + \frac{2\pi}{3}) \\ \sin(\theta) & \sin(\theta - \frac{2\pi}{3}) & \sin(\theta + \frac{2\pi}{3}) \\ \frac{1}{2} & \frac{1}{2} & \frac{1}{2} \end{pmatrix} \quad (12)$$

B. Phase Locked Loop (PLL)

A Phase Locked Loop (PLL) system is required for orienting the converter controllers with the grid angle [17]. The synchronous reference frame is oriented with the d-axis voltage employing a PI regulator. The output of this controller is the estimated frequency of the grid, which is integrated to obtain the angle for the system Park transformations. The PI regulator included in the PLL is:

$$K_{pll} = \frac{(k_{p-pll}s + k_{i-pll})}{s} \quad (13)$$

where k_{p-pll} and k_{i-pll} are the proportional and integral gains of the regulator, calculated based on the amplitude of the AC voltage and the bandwidth desired for the PLL [17]. The inner dynamics of the PLL system introduce an angle deviation between the real grid angle and the estimated angle, specially during voltage transients. In order to introduce this effect into the converter linear model, the PLL tracking system can be linearized as [14], [18]:

$$\Delta e_\theta = -\frac{k_{p-pll}s + k_{i-pll}}{s^2 + u_0^q k_{p-pll}s + u_0^q k_{i-pll}}\Delta u^d \quad (14)$$

where e_θ is the angle deviation between the grid angle, and the PLL estimated angle and u_0^q is the voltage of the q axis at the linearization point. Besides, the existing deviation between the grid real and estimated angles, must be integrated into the model variables. This effect is included as a rotation of the angle deviation between both angles. Then, two different synchronous reference frames variables are defined, the x^{qd} (x^q and x^d) variables corresponding to the synchronous reference calculated from the grid angle, and the x^{qdc} (x^{qc} and x^{dc}) variables related to the synchronous reference frame calculated from the PLL estimated angle. The transformation $\mathbf{T_c^{qd}}$ relates both references:

$$\Delta x^{qdc} = \mathbf{T_c^{qd}} \left(\Delta x^q, \Delta x^d, \Delta e_\theta\right)^T \quad (15)$$

where $\mathbf{T_c^{qd}}$ is:

$$\mathbf{T_c^{qd}} = \begin{pmatrix} \cos\left(e_{\theta_0}\right) & -\sin\left(e_{\theta_0}\right) & -\sin\left(e_{\theta_0}\right) x_0^q - \cos\left(e_{\theta_0}\right) x_0^d \\ \sin\left(e_{\theta_0}\right) & \cos\left(e_{\theta_0}\right) & \cos\left(e_{\theta_0}\right) x_0^q - \sin\left(e_{\theta_0}\right) x_0^d \end{pmatrix} \quad (16)$$

where e_{θ_0} is the angle error deviation value at the linearization point and x_0^d and x_0^q are the x^{qd} components magnitudes around at the linearization point. Also, the inverse transformation can be defined as:

$$\Delta x^{qd} = \mathbf{T_c^{qd^{-1}}} \left(\Delta x^{qc}, \Delta x^{dc}, \Delta e_\theta\right)^T \quad (17)$$

where $\mathbf{T_c^{qd^{-1}}}$ is:

$$\mathbf{T_c^{qd^{-1}}} = \begin{pmatrix} \cos\left(e_{\theta_0}\right) & \sin\left(e_{\theta_0}\right) & \cos\left(e_{\theta_0}\right) x_0^d - \sin\left(e_{\theta_0}\right) x_0^q \\ -\sin\left(e_{\theta_0}\right) & \cos\left(e_{\theta_0}\right) & -\cos\left(e_{\theta_0}\right) x_0^q - \sin\left(e_{\theta_0}\right) x_0^d \end{pmatrix} \quad (18)$$

C. Current control

The current loop (CL) is based on the conventional vector control strategy [19]. It is based on two different PI regulators G_{CL} besides a decoupling loop, as it is shown in Fig. 4. The current loop is implemented in x^{qdc} variables.

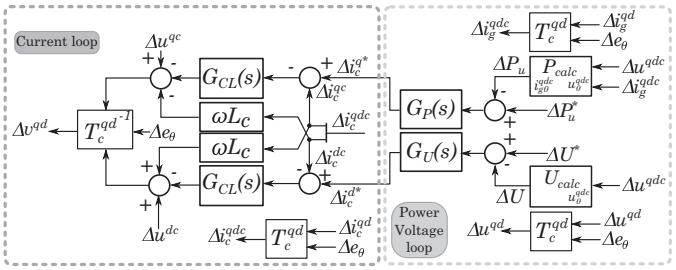

Figure 4. Current loop and power and voltage loops linearized structures

D. Power and voltage control

The power and voltage controllers are implemented by two different regulators (G_P and G_U), as it is shown in Fig. 4. Typically, both controllers are conventional PI regulators [5]. The power and voltage feedback signals must be linear to be included into the model, then both magnitudes are calculated employing x^{qdc} converter variables:

$$\Delta P_u = \frac{3}{2}\left(\Delta i_g^{qc} u_0^q + i_{g0}^q \Delta u^{qc} + \Delta i_g^{dc} u_0^d + i_{g0}^d \Delta u^{dc}\right) \quad (19)$$

$$\Delta U = \frac{u_0^q \Delta u^{qc}}{\sqrt{(u_0^q)^2 + (u_0^d)^2}} + \frac{u_0^d \Delta u^{dc}}{\sqrt{(u_0^q)^2 + (u_0^d)^2}} \quad (20)$$

E. Multi-terminal DC grid system modeling

First, a connection between two DC grid terminals $i - j$ (Fig. 5), is used to illustrate how to obtain the linearized grid model of the DC system. The cable is modeled using a π-equivalent model, in which the capacitors at both ends are the result of adding all the capacitors connected in parallel at those points. Next, the differential equations of the generic link are obtained:

$$\frac{dE_i}{dt} = \frac{1}{C_i}(I_i - I_{Lij}) = \frac{1}{C_i}(\frac{P_i}{E_i} - I_{Lij}) \quad (21)$$

$$\frac{dE_j}{dt} = \frac{1}{C_j}(I_{Lij} - I_j) = \frac{1}{C_j}(I_{Lij} - \frac{P_j}{E_j}) \quad (22)$$

$$E_i - E_j = R_{ij} I_{Lij} + L_{ij} \frac{dI_{Lij}}{dt} \quad (23)$$

where E_i and E_j are the voltages at the equivalent capacitors, I_i and I_j are the currents flowing through the converter, P_i and P_j are the input/output power flowing through the converters, I_{Lij} is the current flowing through the line, C_i and C_j are the equivalent capacitances at both sides of the DC link and R_{ij} and L_{ij} are the equivalent cable resistance and inductance of the π-equivalent model. Due to the division between variables, the expression of the DC current should be linearized to be included in the model, as it is shown next for the node i:

$$I_i = \frac{P_i}{E_i} \approx \frac{\Delta P_i}{E_{i0}} - \frac{P_{i0}}{E_{i0}^2}\Delta E_i \quad (24)$$

where ΔE_i and ΔP_i are linearized variables representing the voltage at the node i and the power flowing through the converter i, respectively. Also, E_{i0} and P_{i0} are the power and the voltage at the linearization point. Finally, combining the previous expressions, the DC link state-space representation can be obtained.

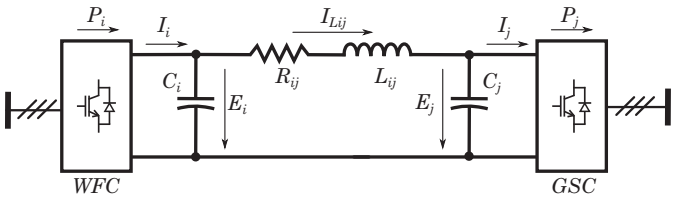

Figure 5. DC connection between two nodes of the multi-terminal grid

This model can be extended to a more complex multi-terminal grid, deriving the equivalent circuit of the DC grid and obtaining the system equations as explained above. Then, the linear state-space of DC grid model, obtained based on the grid equations is:

$$\begin{aligned} \frac{d\Delta x}{dt} &= \mathbf{A}\Delta x + \mathbf{B_u}\Delta u + \mathbf{B_w}\Delta w, \\ \Delta y &= \mathbf{C_y}\Delta x, \quad \Delta z = \mathbf{C_z}\Delta x, \end{aligned} \quad (25)$$

where Δx is the state vector, Δu and Δw are the controlled and non-controlled inputs, Δy and Δz are the controlled and non controlled outputs, and $\mathbf{A}$, $\mathbf{B_u}$, $\mathbf{B_w}$, $\mathbf{C_y}$ and $\mathbf{C_z}$ are matrices of suitable dimensions. These matrices are obtained after arranging the variables and applying matrix computation laws. Typically, in electrical systems, the inductor currents and the capacitor voltages are selected as state variables. Then, for a generic multi-terminal grid, the state vector is:

$$\begin{aligned} \Delta x = (&\Delta E_1, \cdots, \Delta E_n, \Delta E_{n+1}, \cdots \\ &\cdots, \Delta E_{n+m}, \Delta I_{L_1}, \cdots, \Delta I_{L_p})^T \end{aligned} \quad (26)$$

where n is the number of GSCs performing droop control, m the number of wind farms and p the number of branch interconnections (previously defined as $i - j$). The controlled and non controlled inputs u and w, and the controlled and non controlled outputs y and z, can be expressed as:

$$\begin{aligned} \Delta u &= (\Delta P_1, \ldots, \Delta P_n)^T, \quad \Delta w = (\Delta P_{n+1}, \ldots, \Delta P_{n+m})^T \\ \Delta y &= (\Delta E_1, \ldots, \Delta E_n)^T, \quad \Delta z = (\Delta E_{n+1}, \ldots, \Delta E_{n+m})^T \end{aligned} \quad (27)$$

Notice that Δu and Δy are variables related with the GSCs, that are controlling the DC voltage, whereas Δw and Δz are variables related with the WFCs, where the voltage is not controlled. Finally, the presented AC side and DC grid linear models can be combined in order to build a complete linear model of the multi-terminal grid, as it is shown in Fig. 6. Note that, only the node i AC dynamics are represented in the figure for simplicity.

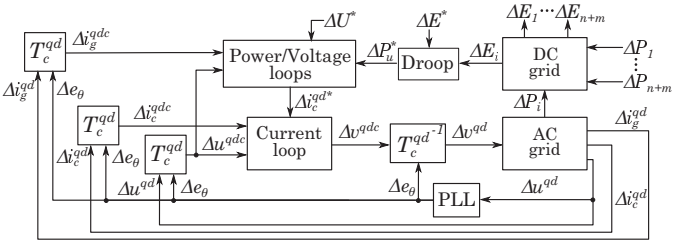

Figure 6. Complete linear model of the multi-terminal grid

IV. Control design methodology

In this section, a theoretical procedure for designing a droop control for multi-terminal grids is addressed. As it is explained in Section II, the droop control behavior not only depends on the DC or AC grid dynamics, but also on the inner control loops of the converter (Fig. 7). Then, a procedure to design both the inner control loops and the droop voltage control loop is presented.

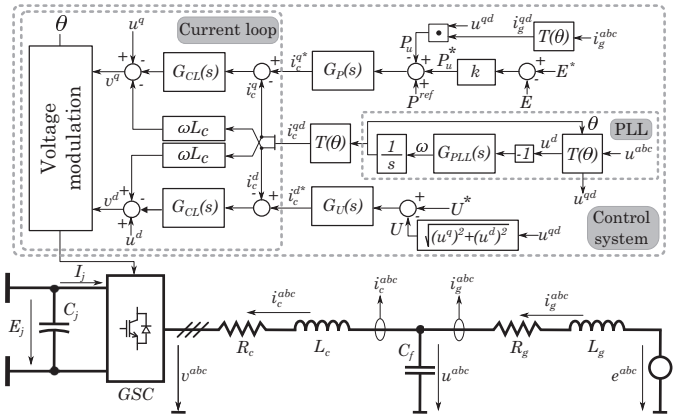

Figure 7. Converter control scheme

A. Current control loop

The inner current control is based on vector control in the synchronous reference frame, tuned by Internal Model Control (IMC) technique [19]. Therefore, two PI regulators (G_{CL}) plus a decoupling loop are employed to track the x^{qd} current references in a defined time, following a first order system response with a time constant τ:

$$K_c = \frac{k_p s + k_i}{s}, \quad k_p = \frac{L_c}{\tau}, \quad k_i = \frac{R_c}{\tau} \tag{28}$$

The control closed loop time constant τ can be calculated based on the desired settling time, which physically represents the time that the system response takes to settle within a range of the final value (usually $\pm 5\%$ or $\pm 2\%$ depending on the criterion). The current loop settling time is typically selected to track current references within a few milliseconds. Saturations are included in the control scheme, in order not to exceed the maximum current rating of the converter.

B. Power and voltage loop

As it is shown in Fig. 7, two different controllers, one for tracking power references (G_P) and another to regulate the AC grid voltage (G_U), are introduced as an outer loop of the current vector control. As the power loop is receiving references from the droop voltage loop, fast dynamics could be required to respond to voltage variations in the DC grid. Therefore, the bandwidth for the outer loop controller should be designed to follow relatively fast droop control outputs without disturbing the inner current control loop. For this reason, the AC side of the linear model of the system (Fig. 6) is employed to design G_P and G_U, considering the dynamics of the inner current loop. The parameters of both controllers are calculated based on optimization robust control techniques [15], [20]. The inputs for the optimization are basically the desired settling time for reference tracking for both controllers, expressed as two different objective transfer functions. Then, the optimization algorithm is run to design the PI parameters based on the frequency requirements.

C. Droop control

The droop design should be carried out considering all the dynamics of the multi-terminal system, as these affect the performance of the controller. For this reason, the control analysis should employ the linear model of the multi-terminal grid explained above, which includes the different systems involved in the droop operation. The complete dynamic system of the multi-terminal grid is depicted in Fig. 8, where the different control stages of the converter can be identified.

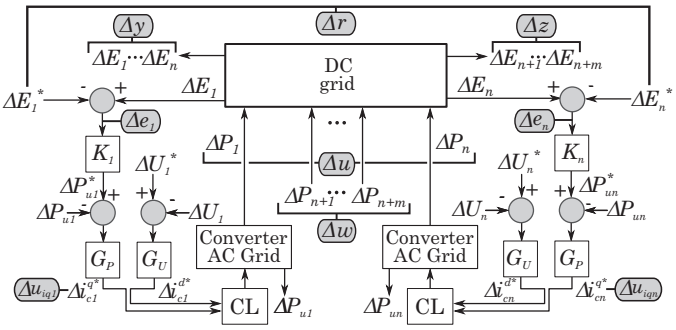

Figure 8. HVDC grid control scheme

Fig. 8 is redrawn in a conventional feedback structure in Fig. 9, showing the control design problem to be addressed. Based on this scheme, different closed loop transfer function matrices can be calculated combining the converters and both AC and DC grid dynamics:

$$\begin{aligned}
&\Delta e(s) = \Delta y(s) - \Delta r(s) = (E_w(s) \quad E_r(s))\Delta v(s)\\
&\Delta u_{iq}(s) = (U_w^{u_{iq}}(s) \quad U_r^{u_{iq}}(s))\Delta v(s)\\
&\Delta v(s) = (\Delta w(s) \quad \Delta r(s))^T\\
&\Delta r(s) = (\Delta E_1^*, \cdots, \Delta E_n^*)^T\\
&\Delta u_{iq}(s) = (\Delta i_{c1}^{q*}, \cdots, \Delta i_{cn}^{q*})^T
\end{aligned} \tag{29}$$

where $E_r(s)$ and $E_w(s)$ are the transfer function matrices, relating the droop voltage references r and the power introduced in the HVDC grid by the wind farms w, with the system voltage errors e at the controlled nodes, respectively. Analogously, $U_r^{u_{iq}}(s)$ and $U_w^{u_{iq}}(s)$ relate the droop references r and the wind farm incoming power w, with the active current loop references u_{iq} of the current loop of the different converters.

The different droop controller constants can be designed analyzing the frequency response of the multi-variable system transfer function matrices, using the singular values representation. This technique can be understood as an expansion of the Bode frequency representation for multi-variable systems. Basically, the specifications for the different droop controllers are the desired power sharing among the different converters controlling the DC voltage, the maximum voltage error allowed at the grid terminals and the maximum converter current ratings. These requirements can be transferred as gain

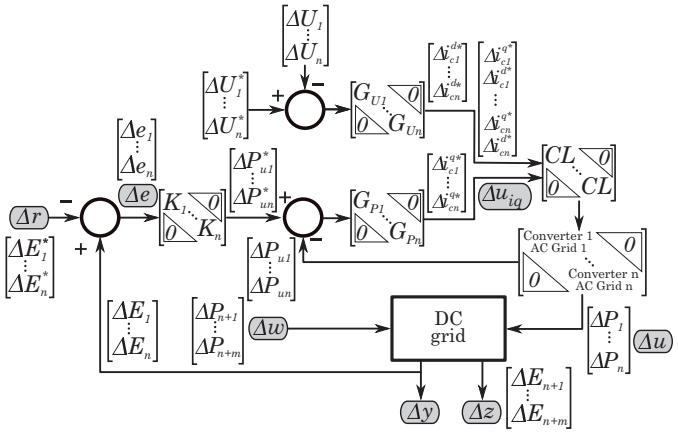

Figure 9. HVDC multi-terminal grid control structure

boundaries in the multi-variable frequency response of the overall system [9]. In order to perform the frequency analysis, the structure of the droop controller is defined as:

$$K = \begin{pmatrix} K_1 & & 0 \\ & \ddots & \\ 0 & & K_n \end{pmatrix} = K_g \begin{pmatrix} q_1 & & 0 \\ & \ddots & \\ 0 & & q_n \end{pmatrix} \tag{30}$$

where K_n are the droop constants implemented in each of the GSCs, K_g is a generic scale factor and q_1 to q_n are the weights of the different controllers, that can be calculated based on the power sharing [9]. Then, in order to dynamically analyze the system, only the parameter K_g needs to be selected, assuming that the q_n constants are defined based on the desired power sharing [7]. However, according to [21] scaling the parameter K_g, maintaining the different q_n values constant, could cause deviations on the desired power sharing between converters. In this article, it is assumed that this deviations can be compensated by the secondary control [4]. However, if the power deviation obtained is too large, the droop design solution could be based on performing an analysis of the control dynamics, modifying the q_n parameters as the K_g introduced is changed, in order to maintain the power sharing.

Assuming the previous considerations, the singular values representation of the system transfer function matrices of the system can be obtained as:

$$\sigma_i(G(j\omega)) = \sqrt{\lambda_i(G^T(j\omega)G(j\omega))} \tag{31}$$

where $\lambda_i(\cdot)$ is the i-th eigenvalue of the matrix. This calculation shows how a system vector input is seen at the output. Specifically, for a defined frequency, the maximum singular value $\bar{\sigma}(G(j\omega))$ is extremely interesting, as it shows the possible maximum amplification that the system is applying to an input vector oscillating at this frequency [22]. This calculation could be extended for the whole range of frequencies, obtaining the singular values frequency representation of a transfer function matrix. Then, assuming a defined power sharing, the control objectives can be focused on minimizing the voltage errors without exceeding the converter current limitations. As it is mentioned above, these requirements can be imposed as boundaries on the singular values frequency response, that could limit the maximum and minimum values of K_g. For example, the maximum energy of the error, caused by any input v of bounded energy, is given by:

$$\max_{v \neq 0} \frac{\|e\|_2}{\|v\|_2} = \max_{\omega} \bar{\sigma}(T_{ev}(j\omega)) \tag{32}$$

where $\|e\|_2^2 = \int e^T e \, dt$ is the 2-norm of e. Therefore, to minimize the effects of the disturbance w on the voltage error e can be understood as minimizing:

$$\bar{\sigma} \begin{pmatrix} E_w(s) & E_r(s) \end{pmatrix} \tag{33}$$

and to maintain the control flowing through the converter under the defined limits can be expressed as ensuring that

$$\bar{\sigma} \begin{pmatrix} U_w^{u_{iq}}(s) & U_r^{u_{iq}}(s) \end{pmatrix} \tag{34}$$

is bounded at the frequencies of interest.

D. DC oscillation damping loop

The power and voltage loops are tuned in the range of tens of milliseconds in order not to interact with the lower level current controllers, designed to respond within a few milliseconds. Considering the presented control structure (Fig. 7), as the droop controller output is connected to the power loop input, certain fast power transients could cause variations of the voltage due to the grid behavior, that could not be properly damped, considering the limited bandwidth of the power loop.

A modification of the presented control scheme (Fig. 7) is shown in Fig. 10. A compensator between the voltage error and the active current reference is included to damp fast voltage variations of the system, as the current loop has a higher bandwidth compared to the power loop. The suggested compensator is based on a band-pass filter, which does not modify the power sharing in steady state established by the droop control. It should be tuned to act within the frequency range between power regulator and the current regulator bandwidth. The filter can be designed as:

$$G_{bp} = K_{bp} \frac{t_1 s}{t_1 s + 1} \frac{1}{t_2 s + 1} = K_{bp} G_f \tag{35}$$

where K_{bp} is the gain of the band-pass filter and t_1 and t_2 are the time response constants of the high-pass and low-pass filters respectively, compounding the band-pass. If t_1 and t_2 are selected to be the time constant of the power loop and the current loop respectively, the band pass-filter will not interfere in the operation of the mentioned controllers. Also, if different converters include this oscillation damping loop within a multi-terminal grid, different tuning of the filter gains K_{bp} could allow to establish an oscillation damping effect sharing between the grid converters, acting similarly as the droop voltage in the defined range of frequencies. Thus, the filter gain could be selected to impose which of the grid converters absorbs a higher percentage of the DC grid voltage oscillations. The multi-variable compensator is defined as:

$$K_d = \begin{pmatrix} K_{bp1} G_f & & 0 \\ & \ddots & \\ 0 & & K_{bpn} G_f \end{pmatrix} = K_f \begin{pmatrix} d_1 G_f & & 0 \\ & \ddots & \\ 0 & & d_n G_f \end{pmatrix} \tag{36}$$

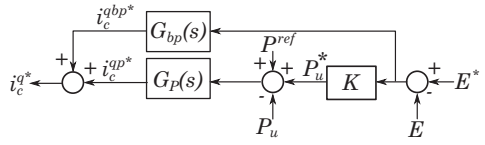

Figure 10. Droop and power loop combined with the DC oscillation damping

where K_f is a generic scale factor and d_1 to d_n are the weights of the different compensation loops. Specifically, values from d_1 to d_n can be defined based on the oscillation sharing desired for each GSC, analogously to the droop power sharing parametrization. Thus, selecting the K_f constant, the controller becomes completely defined. In order to select the mentioned parameter, the singular values of the system transfer function matrices can be analyzed, including the damping loop in the matrix transfer functions calculations.

V. Case study

The analyzed HVDC system consists of a three node multi-terminal VSC-HVDC scheme (Fig 11). Two power converters are connected to the AC grid (GSC 1 and GSC 2) and the other is connected to a wind farm (WFC 3). The parameters used for the study are shown in Tables I and II. The proposed system is analyzed assuming that droop voltage control is carried out by both GSCs, whereas the WFC is supposed to inject all the generated power from the wind power plant. It is considered that both GSCs are connected to two different grids under equivalent conditions. The different controllers involved in the system are designed following the methodology described in Section IV.

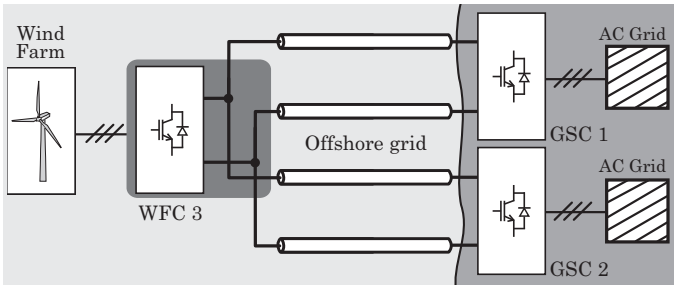

Figure 11. Three-terminal VSC-HVDC grid

Table I
Parameters of the three-terminal DC grid. CIGRÉ B4 DC grid test system [5]

DC grid parameters	Value	Units
Line resistance R	0.0095	Ω/km
Line inductance L	2.112	mH/km
Line capacitance C	0.1906	μF/km
Cable distance 13 d_{13}	100	km
Cable distance 23 d_{23}	150	km
GSC/WFC DC link capacitor C_{dc}	150	μF
GSC rated power P_1, P_2	350	MW
WFC rated power P_3	700	MW
Reference voltage E^*	400	kV

Table II
Parameter of the AC side converters [14]

AC side parameters	Value	Units
Nominal Power P_1, P_2	350	MW
Nominal Voltage V_{ac}	195	kV
Short Circuit ratio (SCR)	5	-
Grid Thévenin Xn/Rn ratio	10	-
Coupling inductance L_c	0.2	pu
Coupling resistance R_c	0.01	pu
Capacitor filter impedance X_f	5.88	pu

First, the grid state-space model is obtained. The defined state variables Δx, input signals Δu and Δw, and output signals Δy and Δz are:

$$\Delta x = (E_1,\ E_2,\ E_3,\ I_{L13},\ I_{L23}) \tag{37}$$

$$\Delta u = (\Delta P_1,\ \Delta P_2) \quad \Delta w = (\Delta P_3) \tag{38}$$

$$\Delta y = (\Delta E_1,\ \Delta E_2) \quad \Delta z = (\Delta E_3) \tag{39}$$

and the linearized state-space matrices are:

$$\mathbf{A} = \begin{pmatrix} -\frac{P_{10}}{C_1 E_{10}^2} & 0 & -\frac{1}{C_1} & 0 & 0 \\ 0 & -\frac{P_{20}}{C_2 E_{20}^2} & 0 & 0 & -\frac{1}{C_2} \\ 0 & 0 & +\frac{P_{30}}{C_3 E_{30}^2} & \frac{1}{C_3} & \frac{1}{C_3} \\ \frac{1}{L_{13}} & 0 & -\frac{1}{L_{13}} & -\frac{R_{13}}{L_{13}} & 0 \\ 0 & \frac{1}{L_{23}} & -\frac{1}{L_{23}} & 0 & -\frac{R_{23}}{L_{23}} \end{pmatrix} \tag{40}$$

$$\mathbf{B_u} = \begin{pmatrix} \frac{1}{C_1 E_{10}} & 0 \\ 0 & \frac{1}{C_2 E_{20}} \\ \hline \mathbf{0_{3x2}} \end{pmatrix} \mathbf{B_w} = \begin{pmatrix} \mathbf{0_{2x1}} \\ \hline -\frac{1}{C_3 E_{30}} \\ \hline \mathbf{0_{2x1}} \end{pmatrix} \tag{41}$$

$$\mathbf{C_y} = \left(\begin{array}{c|c} \mathbf{I_{2x2}} & \mathbf{0_{2x3}} \end{array} \right), \quad \mathbf{C_z} = \left(\begin{array}{c|c|c} \mathbf{0_{1x2}} & 1 & \mathbf{0_{1x2}} \end{array} \right) \tag{42}$$

Once the DC grid state-space model is derived, the AC system models for both converters are also obtained. Then, the inner current controller is designed to track references with a settling time of 10 ms [23], based on IMC. It has been observed, that the AC grid voltage measured at the capacitors u^{qd} can be importantly affected during a fast active current change, specially for grids with low SCR. As this voltage is employed for the decoupling loop, a low pass filter is applied to the u^{qd} measurement in order not to introduce these fast dynamics into the controller [14]. This low pass filter can be tuned to be around ten times faster than the current loop.

Having defined the current controller, the power and voltage loop PI controllers are designed based on the linear model (Fig. 6) applying robust control tuning techniques [15], [20]. The settling time is defined to be approximately 100 ms for both power and voltage regulators [23]. The output of the robust optimization parametric design is shown in Fig. 12a, where the closed loop transfer functions of the power and voltage control are depicted, showing an acceptable performance. Also, a comparison between the complete simulation model and the linear model, derived to design the different controllers, is shown in Fig. 12b. This comparison shows that the differences between both models are minimum, thus validating the use of the linear model for control design purposes.

Analogously to the current loop, low pass filters are applied to the voltage u^{qd} and currents i_g^{qd} measurements employed for calculating the power and voltage feedback measurements, in order to damp fast transients of the magnitudes. These low pass filters can be also tuned around ten times faster than the current loop.

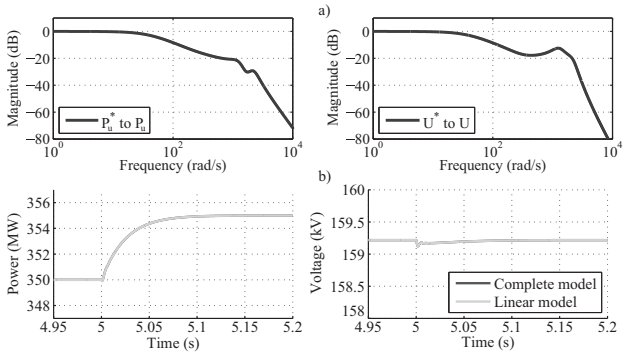

Figure 12. Design output of the voltage and power loops of the converter. a) Bode representation of the closed loop transfer functions (P_u^* to P_u and U^* to U). b) Power and voltage response comparison between the complete and linear models, for a power step change.

Once the outer power and voltage loops are designed, the multi-terminal droop control is addressed. Assuming that the power generated by the wind power plant, injected to the DC grid by the WFC, must be shared by both GSCs, an initial parametrization is established for the controller. Then, the multi-variable droop controller, considering that GSC 1 and GSC 2 are regulating the voltage, can be defined as:

$$\mathbf{K} = \begin{pmatrix} K_1 & 0 \\ 0 & K_2 \end{pmatrix} = K_g \cdot \begin{pmatrix} 1 & 0 \\ 0 & 1 \end{pmatrix} = K_g \cdot \mathbf{I_2} \qquad (43)$$

where K_1 and K_2 are the droop constants locally implemented at each of the GSCs, expressed in kW/V units. This parametrization could lead to an unequal power sharing, depending on the grid impedances and the power flow, fact that can be solved by the secondary control. Then, as the exact power sharing is ensured by the upper control layer, this work is focused on the design of the droop control considering the dynamics of the whole multi-terminal grid. Then, based on the linear model of the system, the transfer function matrices $E_w(s)$, $E_r(s)$, $U_w^{u_{iq}}(s)$ and $U_r^{u_{iq}}(s)$ are obtained following the structure shown in Fig. 9. Note that, the reference inputs E^* do not introduce any voltage error in the system [9], thus the system analysis will only be focused on $E_w(s)$ and $U_w^{u_{iq}}(s)$, that relate the voltage errors and the control action with the wind power input, respectively.

Next, the singular values representation of $E_w(s)$ relating the GSC DC voltage errors and the power coming from the wind farm is depicted in Fig. 13a. Assuming a maximum voltage error of a 10% of the nominal value at each terminal. The singular values representation should not exceed, in steady state, a maximum gain of [9]:

$$\bar{\sigma}(E_w(0)) \leq \frac{||e(0)||_2}{||w(0)||_2} = 20\log_{10}\left(\frac{\sqrt{(e_{mx1}+e_{mx2})}}{P_3}\right) =$$
$$= 20\log_{10}\left(\frac{\sqrt{(4\cdot 10^5 \cdot 0.1)^2 \cdot 2}}{700\cdot 10^6}\right) = -81.85 \text{ dB} \qquad (44)$$

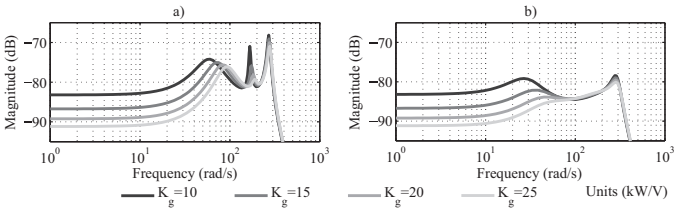

Figure 13. Singular values representation of $E_w(s)$ (DC voltage errors - Wind power input) a) Without oscillation damping, b) With oscillation damping.

According to Fig. 13a, all the droop constants K_g depicted are able to maintain the maximum voltage error below a 10% of the nominal voltage value, in steady state. However, resonance peaks are observed at relatively low frequencies, fact that could cause voltage oscillations during wind power flow variations, specially if the wind farm power input excites those frequencies. In order to damp those peaks, the DC oscillation damping loop is implemented in both GSCs setting t_1 and t_2 at the time constants of the current and the power loop respectively. For a first analysis, the same gain is applied to both filters, considering a K_f equal to 1/20 A/V.

Fig. 13b shows again the frequency response of $E_w(s)$, including the designed oscillation damping loop. This graph shows that the gain peaks have been reduced, confirming that the oscillation damping loop is able to improve the droop control performance. Moreover, as the damping effect can be shared between the different GSC converters, Fig. 14 is drawn to show how different weights d_1-d_2 affect the overall grid voltage error, as:

$$K_d = \begin{pmatrix} K_{bp1}G_f & 0 \\ 0 & K_{bpn}G_f \end{pmatrix} = \begin{pmatrix} d_1G_f & 0 \\ 0 & d_2G_f \end{pmatrix} \qquad (45)$$

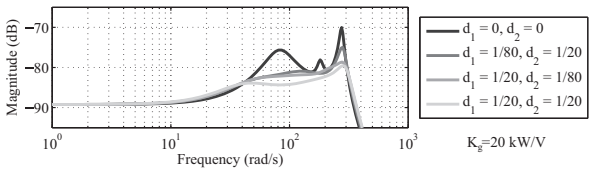

Figure 14. Singular values representation of $E_w(s)$ (DC voltage errors - Wind power input), for different damping loops.

Fig. 14 shows that the maximum gains, and consequently the maximum voltage error, are obtained disconnecting the damping loop (d_1 and d_2 equal to 0). On the other hand, the minimum voltage error is achieved when both converters include the same oscillation damping loop. Moreover, two intermediate cases are shown, where the damping loop of one of the two GSC converters, has a higher filter gain compared to the other. Both cases show a gain reduction

compared to the system without damping loop, revealing that the overall grid error can be compensated acting from different nodes. However, one of the intermediate cases shows lower gain peaks compared to the other. This fact is caused by the difference between the line impedances, which allows to one of the GSCs to apply a greater damping effect on the overall grid oscillation damping. This analysis reveals that the damping loop is not only locally affecting the node where it is implemented, but also the overall grid voltage oscillations.

From now on, it is considered that the gain of the damping loop at both GSCs is equal (d_1=d_2=1). Thus, setting the gain K_f, the damping controller is defined. Then, an extended analysis of the singular values of the transfer function $E_w(s)$, considering several droop constants K_g and including different oscillation damping loops K_f, is shown in Fig. 15.

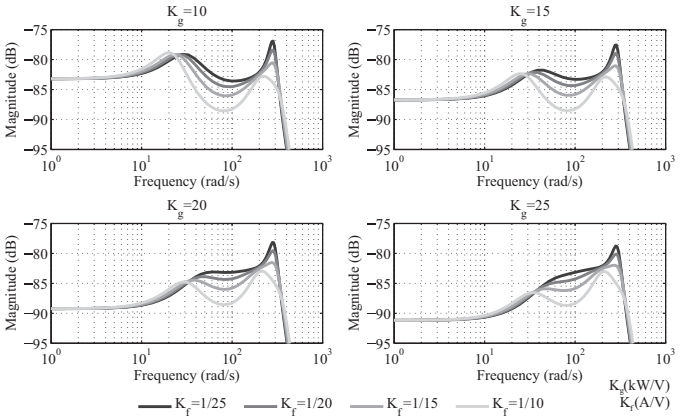

Figure 15. Singular values representation of $E_w(s)$ (DC voltage errors - Wind power input), including damping loop, for different K_g and K_f.

Also, the singular values representation of the transfer function matrix $U_w^{u_{iq}}(s)$, relating the control action (represented by the current loop references) and the power coming from the wind farms, is depicted in Fig. 16 for several droop constants K_g and different oscillation damping loops K_f.

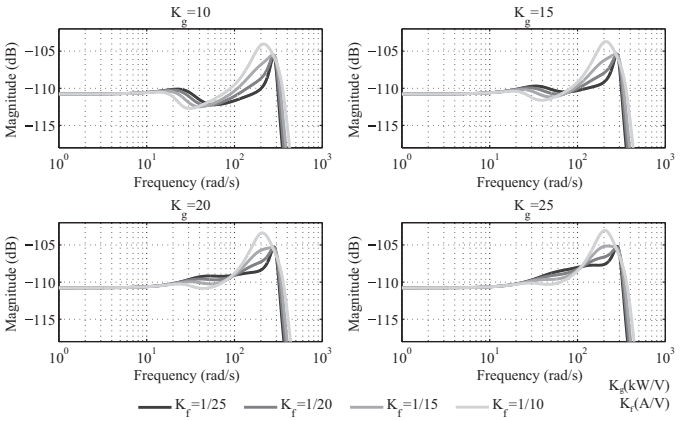

Figure 16. Singular values representation of $U_w^{u_{iq}}(s)$ (Current loop references - Wind power input), including damping loop, for different K_g and K_f.

Figs. 15 and 16 must be analyzed together in order to decide which are the most favorable constants K_g and K_f for the system. First, analogously to the gain limitation imposed to the frequency response of $E_w(s)$, another limitation is calculated for the singular values of $U_w^{u_{iq}}(s)$, considering that the maximum allowed current that could flow through the converter is a 110% of the nominal current value. This corresponds to a gain boundary limitation of -109.74 dB.

Before analyzing the singular values, it should be mentioned that the power loop of the WFC is considered to respond with the same bandwidth as the GSC. Then, power disturbances with frequencies larger than approximately 40 rad/s will not be introduced into the system, unless an AC fault occurs in the wind farm. In that case, the WFC could reduce the power injected to the DC grid rapidly to zero.

Fig. 15 shows that constants K_g greater than 15 kW/V with K_f also greater than 1/15 A/V allow to operate the system maintaining the voltage error under the defined 10%. Besides, as the system wind power disturbances are limited in bandwidth, the error can even be maintained below a 5%. To achieve this goal, the GSCs need to inject current to the grid (control action) without exceeding its own limits. Then, the singular values gains of $U_w^{u_{iq}}(s)$, shown in Fig. 16, should be maintained below the calculated boundary. It can be seen that all curves exceed the maximum allowed gain at a certain frequency, which is not desirable from the converter operation perspective. Specifically, certain combinations of K_g and K_f present gain curves that are crossing the defined boundary below the power loop bandwidth (40 rad/s), which could lead the converter to operate out of its limits. For this reason, constants K_g higher than 20 kW/V should not be included in the control system. Finally, in order to select the controller constants, among the different possible available combinations, the defined criterion is to minimize the voltage error, while maintaining the converter operating within its current limits. Based on this criteria, constants K_g of 20 kW/V and K_f of 1/20 A/V are able to securely operate the system minimizing the error, without exceeding the current limitation.

Once the droop control design is concluded, Matlab-Simulink® simulations of the three-terminal grid (Fig. 11) are carried out to validate the obtained results. Figs. 17 and 18 show the voltage droop control response (performed by the GSCs) to a nominal power input from the WFC from 0 MW to 700 MW at 2 s. During the simulation, the power reference of both GSC P_{ref} is maintained at zero, in order to observe how the designed distributed droop controller is able to control the overall DC voltage without communications. The cable model employed is a π-equivalent model with 100 sections. Fig. 17 shows that both GSCs accomplish the power sharing condition, because both are extracting approximately the same amount of power, despite the variations introduced by the different cable longitudes. This deviation could be compensated by the secondary control. It can also be observed that no voltage error is present when no power is flowing through the grid.

Focusing on the dynamics, during the power transient, the voltage is maintained below the 10% of maximum error defined, even below a 5%. Also, the current do not exceed the defined converter limits. Then, the presented simulations show that the control design is able to operate the system avoiding large variations both in the AC and the DC side variables, maintaining the converters operation within their limits.

The same simulation is carried out without including the damping compensation loop in both converters, in order to analyze the system behavior. Fig. 18 shows that without including this compensation, the oscillations in all system variables increase compared to Fig. 17, confirming the effectiveness of the damping loop.

Fig. 19 shows a fast power reduction introduced by the WFC caused by an AC fault in the wind farm grid. The power injected from the wind farm is rapidly reduced to zero at 4 s. Large oscillations in voltage and current can be seen due to the fast power reduction. This can be explained due to the large gain peaks seen in Figs. 15 and 16 at high frequencies. Therefore, when these peaks are excited due to the fast power reduction, oscillations at those frequencies appear. Despite of this transients, the system reaches the steady state in a few milliseconds without exceeding any limit.

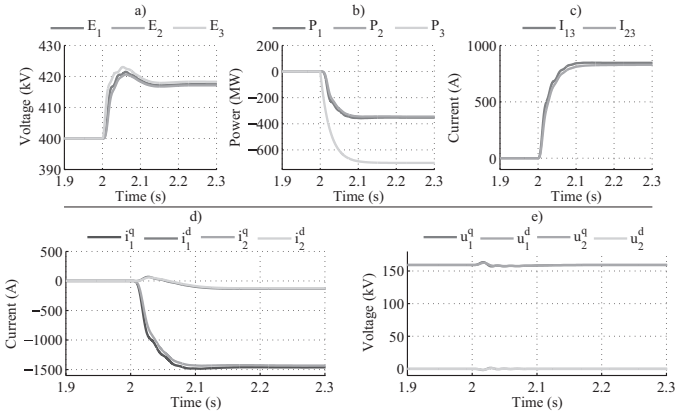

Figure 17. Simulation results after applying a WFC reference step power change. a) DC grid voltages. b) Converters power. c) DC lines current. d) Currents in qd frame. e) PCC voltages in qd frame

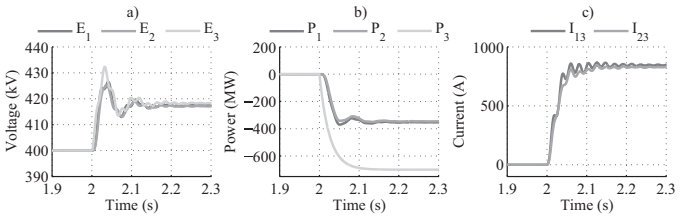

Figure 18. Simulation results after applying a WFC reference step power change without including the damping loop. a) DC grid voltages. b) Converters power. c) DC lines current.

VI. Conclusions

A DC voltage droop design methodology considering the different dynamics involving a multi-terminal VSC-HVDC grid is presented. This methodology includes a procedure for obtaining a linearized model of the complete system. Also, a design criterion for the current loop and the power and voltage loops is provided. Once the inner dynamics of the converter are established, a multi-variable frequency analysis of the droop control performance can be carried out to determine the proper DC droop voltage gains, in order to accomplish the defined system requirements. Also, a controller for damping the oscillations introduced by the system frequency resonances is presented. The global control design procedure is validated through dynamic simulations.

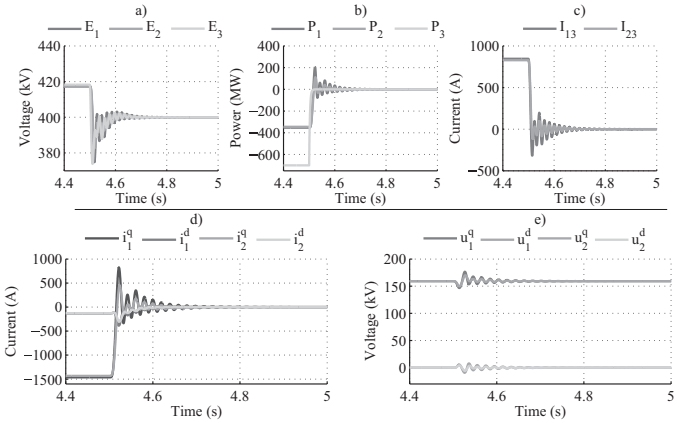

Figure 19. Simulation results after a WFC power reduction - DC grid. a) DC grid voltages. b) Converters power. c) DC lines current. d) Currents in qd frame. e) PCC voltages in qd frame

References

[1] *Europe's onshore and offshore wind energy potential*. Eur. Environmental Agency, Copenhaguen, 2009.

[2] *Wind Energy Technology Roadmap 2013*. Int. Energy Agency, Paris, 2013.

[3] O. Gomis-Bellmunt, J. Liang, J. Ekanayake, R. King, and N. Jenkins, "Topologies of multiterminal HVDC-VSC transmission for large offshore wind farms," *Electric Power Syst. Res.*, vol. 81, no. 2, pp. 271–281, 2011.

[4] A. Egea-Alvarez, J. Beerten, D. V. Hertem, and O. Gomis-Bellmunt, "Primary and secondary power control of multiterminal hvdc grids," *10th IET Int.l Conf. on AC and DC Power Transmission (ACDC 2012)*.

[5] T. K. Vrana, Y. Yang, D. Jovcic, S. Dennetière, J. Jardini, and H. Saad, "The cigre b4 dc grid test system," 2013.

[6] T. K. Vrana, J. Beerten, R. Belmans, and O. B. Fosso, "A classification of dc node voltage control methods for hvdc grids," *Electric Power Syst. Res.*, vol. 103, pp. 137 – 144, 2013.

[7] L. Xu, L. Yao, and M. Bazargan, "DC grid management of a multi-terminal HVDC transmission system for large offshore wind farms," in *Proc. of the Int. Conf. Sustainable Power Generation and Supply (SUPERGEN '09)*, 2009, pp. 1–7.

[8] T. M. Haileselassie and K. Uhlen, "Impact of dc line voltage drops on power flow of mtdc using droop control," *IEEE Trans. Power Syst.*, vol. 27, no. 3, pp. 1441–1449, 2012.

[9] E. Prieto-Araujo, F. Bianchi, A. Junyent-Ferre, and O. Gomis-Bellmunt, "Methodology for droop control dynamic analysis of multiterminal vsc-hvdc grids for offshore wind farms," *IEEE Trans. Power Del.*, vol. 26, no. 4, pp. 2476 –2485, oct. 2011.

[10] X. Zhao and K. Li, "Adaptive backstepping droop controller design for multi-terminal high-voltage direct current systems," *IET Generation, Transmission & Distribution*, 2015.

[11] R. Eriksson, J. Beerten, M. Ghandhari, and R. Belmans, "Optimizing dc voltage droop settings for ac/dc system interactions," *IEEE Trans. on Power Del.*, vol. 29, no. 1, pp. 362–369, Feb 2014.

[12] X. Zhao and K. Li, "Droop setting design for multi-terminal hvdc grids considering voltage deviation impacts," *Electric Power Syst. Research*, vol. 123, pp. 67 – 75, 2015.

[13] O. Gomis-Bellmunt, J. Liang, J. Ekanayake, and N. Jenkins, "Voltage-current characteristics of multiterminal HVDC-VSC for offshore wind farms," *Electric Power Syst. Res.*, vol. 81, no. 2, pp. 440–450, 2011.

[14] L. Zhang, "Modeling and control of vsc-hvdc links connected to systems," Ph.D. dissertation, 2010.

[15] A. Egea-Alvarez, S. Fekriasl, F. Hassan, and O. Gomis-Bellmunt, "Advanced vector control for voltage source converters connected to weak grids," *IEEE Trans. Power Syst.*, vol. PP, no. 99, pp. 1–10, 2015.

[16] C. Ong, *Dynamic Simulation of Electric Machinery: Using MATLAB/SIMULINK*.

[17] S.-K. Chung, "A phase tracking system for three phase utility interface inverters," *IEEE Trans. Power Electron.*, vol. 15, no. 3, pp. 431–438, 2000.
[18] L. Harnefors, M. Bongiorno, and S. Lundberg, "Input-admittance calculation and shaping for controlled voltage-source converters," *IEEE Trans. Ind. Electron.*, vol. 54, no. 6, pp. 3323–3334, Dec 2007.
[19] L. Harnefors and H.-P. Nee, "Model-based current control of ac machines using the internal model control method," *IEEE Trans. Ind. App.*, vol. 34, no. 1, pp. 133–141, Jan 1998.
[20] P. Apkarian and D. Noll, "Nonsmooth h-infinity synthesis," *IEEE Trans. Autom. Control*, vol. 51, no. 1, pp. 71–86, Jan 2006.
[21] J. Beerten and R. Belmans, "Analysis of power sharing and voltage deviations in droop-controlled dc grids," *IEEE Trans. on Power Syst.*, vol. 28, no. 4, pp. 4588–4597, Nov 2013.
[22] S. Skogestad and I. Postlethwaite, *Multivariable feedback control: analysis and design*. Wiley, 1996.
[23] H. Saad, X. Guillaud, J. Mahseredjian, S. Dennetiere, and S. Nguefeu, "Mmc capacitor voltage decoupling and balancing controls," *IEEE Trans. Power Del.*, vol. 30, no. 2, pp. 704–712, April 2015.

Eduardo Prieto-Araujo (S'12) received the degree in Industrial Engineering from the School of Industrial Engineering of Barcelona (ETSEIB), Technical University of Catalonia (UPC), Barcelona, Spain, in 2011, where he is currently pursuing the Ph.D. degree in Electrical Engineering. Since 2010, he has been with the Centre d'Innovació Tecnològica en Convertidors Estàtics i Accionaments, (CITCEA-UPC). His research interests include the modeling and control of electrical machines, renewable generation systems, microgrids and control of power electronic converters for HVDC transmission.

Agustí Egea-Alvarez (S'12-M'15) received the B.S., M.Sc., and Ph.D degrees from the Technical University of Catalonia (UPC), Barcelona, Spain, in 2008, 2010, and 2014, respectively. Now he is with the China Electric Power Research Institute (CEPRI) part of State Grid Corporation of China in Beijing. He has been with the Centre d'Innovació Tecnològica en Convertidors Estàtics i Accionaments, part of the electrical engineering department, in UPC from 2008 to 2015. He is member of IEEE and CIGRE. His current research interests include control and operation of high-voltage direct current systems, DC power flow control converters, renewable generation systems, electrical machines and power converter control.

Sajjad (Fekri) Fekriasl (S'02-M'06) received the B.S.(Hons) and M.S.(Hons) degrees in Electrical Engineering from the University of Tabriz, Iran, in 1995 and 1997, respectively, and the Ph.D. degree in Electrical Engineering and Computer Science from Instituto Superior Técnico (IST), Lisbon, Portugal, in 2006. He has held several technical, leadership and lectureship positions in control systems design for aerospace, automotive, and power systems applications. He was with the Department of Electrical Engineering, University of Leicester, UK (2006-2009) and Lecturer of advanced control and optimisation in School of Engineering, Cranfield University, UK (2010-2012). Since 2012, Dr Fekriasl has joined Smart Grids Research and Technology (SGRT) Division, ALSTOM Grid, Stafford, as Principal Scientist. His current research cover the design of robust multivariable control systems, optimisation and estimation for MMCs, Coordinated FACTS, Wind farm, and MTDC networks control systems. Sajjad is inventor of 5 patents and has published over 47 publications including several journal papers, book chapters and invited papers.

Oriol Gomis-Bellmunt (S'05-M'07-SM'12) received the degree in industrial engineering from the School of Industrial Engineering of Barcelona (ETSEIB), Technical University of Catalonia (UPC), Barcelona, Spain, in 2001 and the PhD in electrical engineering from the UPC in 2007. In 1999 he joined Engitrol S.L. where he worked as project engineer in the automation and control industry. In 2003 he developed part of his PhD thesis in the DLR (German Aerospace center) in Braunschweig (Germany). Since 2004 he is with the Electrical Engineering Department of the UPC where he is lecturer and participates in the CITCEA-UPC research group. Since 2009 he is also with the Catalonia Institute for Energy Research (IREC). His research interests include the fields linked with smart actuators, electrical machines, power electronics, renewable energy integration in power systems, industrial automation and engineering education.